ChemPlusChem

Chemistry Europe
European Chemical Societies Publishing
ChemPlusChem

RESEARCH ARTICLE

Cobalt Phthalocyanine Doping-Induced Electronic Modulation in Metal-Organic Framework-Derived Co_3O_4 and Boosted Alkaline Oxygen Evolution Reaction to Ampere Level

Clara Ghali[1] | Joshuah Tavarez[1] | Paulina Pietrzyk-Thel[2] | Marianna Gniadek[3] | Magdalena Osial[2] | Agata Roszkiewicz[2] | Boka Fikadu[4] | Sohrab Asgaran[5] | Jaebeom Lee[4,6] | Michael Giersig[1] | Justyna Widera-Kalinowska[1] | Nwaji Njemuwa[2]

[1]Department of Chemistry, Adelphi University, Garden City, New York, USA | [2]Institute of Fundamental Technological Research, Polish Academy of Sciences, Warsaw, Poland | [3]Faculty of Chemistry, University of Warsaw, Warsaw, Poland | [4]Department Chemistry, Chungnam National University, Daejeon, South Korea | [5]Helmaco Sp. Z o.o. Company, Warszawa, Poland | [6]Department Chemical Engineering and Applied Chemistry, Chungnam National University, Daejeon, South Korea

Correspondence: Justyna Widera-Kalinowska (widera@adelphi.edu) | Nwaji Njemuwa (nnwaji@ippt.pan.pl)

Received: 6 March 2026 | **Revised:** 17 April 2026 | **Accepted:** 20 April 2026

Keywords: noble-metal free catalyst | oxygen evolution | phthalocyanine doped metal oxide | proton exchange membrane | water electrolysis

ABSTRACT

The oxygen evolution reaction (OER) using noble metal-based catalysts faced significant commercialization challenges due to the scarcity and substantial expense of these noble metals. Thus, the development of an efficient OER electrocatalyst for proton exchange membrane (PEM) water electrolyzers is still a challenging task. Herein, we present a facile approach to preparing cobalt phthalocyanine anchored on N-doped Co_3O_4 carbon network (Co_3O_4-NC) derived from metal organic framework (MOF). This strategy facilitates fast electron transfer and modulates the electronic structure. This improved electron transport induced by CoPc plays a significant role in enhancing OER, requiring only an overpotential of 1.2 V to deliver a current density of 1000 mA cm^{-2} with excellent stability. The Co_3O_4-NC2 Pc catalyst shows excellent durability during PEM water electrolysis and delivers industrially required current density of 1000 mA cm^{-2} at a potential of 1.66 V, outperforming commercial RuO_2. The results of this research are twofold. Firstly, they promote green and low-carbon development. Secondly, they inject new vitality into the development of hydrogen energy technologies.

1 | Introduction

Addressing the growing energy demand has become imperative due to the rapid development of modern human society [1, 2]. However, the excessive use of fossil fuels has had a significant impact on the environment and human health, as it has led to the generation of substantial greenhouse gases [3]. It has become increasingly evident that there is an urgent requirement to harness green renewable energy with a view to ameliorating energy shortages and environmental pollution. The potential of renewable electricity to produce "green hydrogen" via water splitting is widely applied and offers great advantage due to its ability to produce hydrogen with a high degree of purity, flexibility, and zero pollution [4]. The preferred method for producing highly purified hydrogen and oxygen on a large scale is electrocatalytic water splitting, which involves the hydrogen evolution reaction (HER) and the oxygen evolution reaction (OER). However, the electron transfer kinetics during the OER were inherently sluggish, which significantly hampered the efficiency of water splitting [5, 6].

The wide utilization of representative OER catalysts, including RuO_2 and IrO_2, is well-documented [7]. However, the scarcity and high cost of Ir and Ru hinder their potential applications in large-scale hydrogen production [8]. To tackle this problem, the scientific community has been concentrating on creating

low-cost, non-noble metal catalysts that can help to decrease the overpotential under large current densities (LCD). The optimal activity and rapid kinetics of the catalysts created by the researchers were enabled by the manipulation of the physicochemical properties of the intermediates, such as Gibbs free adsorption energy, under favorable conditions [9–12]. However, the conditions in industrial settings involve larger current densities, usually more than 500 mA cm^{-2}, with long working hours that are longer than in laboratory testing conditions. This directly decreases the catalyst activity and long-term stability [13, 14]. To realize commercialization, the integration of the catalysts into electrolytic system is a prerequisite. The anode catalyst layer facilitates the transfer of protons through the proton exchange membrane (PEM) to the cathode, which serves as an electrode for production of high-purity H_2 by the electrons in the cathode collector. Thus, the technology that has the most prevalence in industrial water electrolysis is proton exchange membrane water electrolysis (PEMWE) technology due to its fast dynamic response time, a high purity of H_2, and a more compact design.

The high carbon content in microporous metal organic frameworks (MOFs) renders the material attractive as a precursor for fabrication of carbon-based catalysts [15, 16]. Catalysts with atomically dispersed Co-N_x sites have been identified as efficient in catalyzing OER [17].

Molecular metal phthalocyanine (MPc) is particularly noteworthy due to its malleable electronic configuration and its capacity to function with a plethora of substrates [18, 19]. However, the favorable distribution of electrons around the metal center is hindered by the plane-symmetric structure of MPc, thus affecting the reactant's adsorption [20]. Furthermore, during catalytic operations, the central metal atom of the active site is prone to separation from the MPc, resulting in diminished electrochemical stability [21]. Hence, we can overcome these limitations by introducing MPc species into porous N-doped carbon substrates, as this disrupts the electron symmetry distribution at the metal sites and facilitates adsorption with enhanced stability of the MPc [22]. As a result, the logical design and simple creation of MOF-derived carbon nanomaterials that can efficiently wrap around MPc molecules for effective OER catalysis poses a significant challenge.

Herein, polyhedron and cubic-shaped Co-based metal organic frameworks with nitrogen-containing linkers were thermally transformed into N-doped Co_3O_4 carbon networks (Co_3O_4-NC) and serve as a host matrix for anchoring of cobalt phthalocyanine (CoPc) via π-π stacking (Figure 1). The density functional theory (DFT) calculation reveals a strong interaction of CoPc and Co_3O_4-NC that results in optimization of fast electron transfer and modulation of the electronic bands. We employed the prepared material as an efficient and stable catalyst for OER and anode electrocatalyst for proton exchange membrane (PEM) water electrolysis. The enhanced electron transfer induced by CoPc facilitates OER performance, delivering 10 mA cm^{-2} at an overpotential of 90 mV with a robust stability profile.

2 | Experimental Section

2.1 | Preparation of the Polyhedron-Shaped CoMOF

First, 2.64 g of 2-methylimidazole and 30 mL of methanol were combined in one beaker, followed by mixing with 520 mg of $Co(NO_3)_2{\cdot}6H_2O$ dissolved in 30 mL methanol, and the whole solution was stirred for five min. Next, the obtained purple suspension was left foraging for 24 h at room temperature, so the precipitated polyhedron-shaped CoMOF settled at the bottom of the beaker. After three methanol washes, the obtained material was centrifuged and then dried at 50°C.

2.2 | Preparation of the Cubic-Shaped CoMOF

116 mg of Co $(NO_3)_2{\cdot}6H_2O$ and 2 mg of CTAB were dissolved in 2 mL of de-ionized (DI) water, and the solution was mixed with

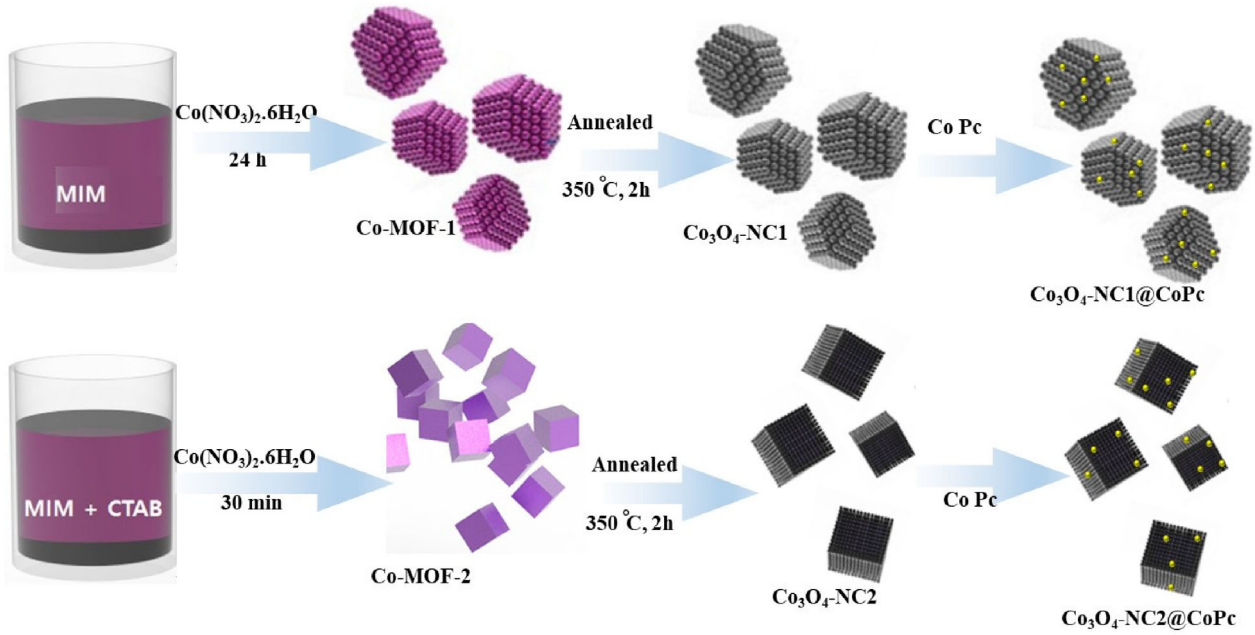

FIGURE 1 | Schematic illustration of the synthetic route for the electrode materials formation.

the already formed solution of 1.82 g of 2-methylimidazole in 25 mL of DI. The solution was stirred for 30 min at room temperature. The purple solid powder was collected by centrifugation and washed with DI water and ethanol at least 3 times. Then, the powder was dried at 50°C.

2.3 | Preparation of CoPc-Doped Co_3O_4-NC

The as-prepared MOFs were annealed in air at 350°C for 2 h, and each were combined with 10 mg of CoPc dissolved in 5 mL of DMF and allowed to stir for 12 h. The solution was centrifuged and washed three times with DMF. The obtained black powder was dried in oven at 70°C.

3 | Results and Discussion

The polyhedron MOF templates were prepared using Co(II) ions and 2-methylimidazole (MIM) as metal nodes and organic linker, respectively, as shown in Figure 1. Incorporation of cetyltrimethylammonium bromide (CTAB) surfactant changes the regular polyhedron morphology to a cubic-shaped MOF template. It has been previously shown that CTABs can surround the seed nuclei formed during MOF growth and alter the crystallographic facet, leading to the formation of nanocubes rather than the commonly observed polyhedron MOF [23]. The annealing of the as-prepared MOFs under atmospheric conditions results in conversion to Co_3O_4 embedded in nitrogen-doped carbon network (Co_3O_4-NC). The synthesis of water-soluble quaternary phthalocyanine (CoPc) follows the previous reported procedure [24]. The as-prepared Co_3O_4-NC was soaked in 1 mL (0.01 M) of CoPc for 20 h, followed by centrifugation to obtain the CoPc-doped Co_3O_4-NC via π-π stacking interactions. For convenience, the Co_3O_4-NC derived from the polyhedron-shaped and cubic-shaped MOFs will henceforth be referred to as Co_3O_4-NC1 and Co_3O_4-NC2, respectively. Similarly, the CoPc-doped analog of Co_3O_4-NC1 and Co_3O_4-NC2 will be referred to as Co_3O_4-NC1 Pc and Co_3O_4-NC2 Pc, respectively.

The panoramic field emission scanning electron microscopy (FESEM) images (Figure S1a,b) for both polyhedron- and cubic-shaped MOFs reveal a highly uniform and monodispersed nanostructure with an average diameter of 550 nm and 150 nm for polyhedron and cubic shape structures, respectively. However, the cubic-shaped MOFs show a rougher surface (Figure S1b). Though the morphologies for both MOFs were conserved following annealing, the surfaces showed more roughness (Figure S1c,d), which could be attributed to defect introduction [25, 26]. Figure 2a,b show the transmission electron microscopy

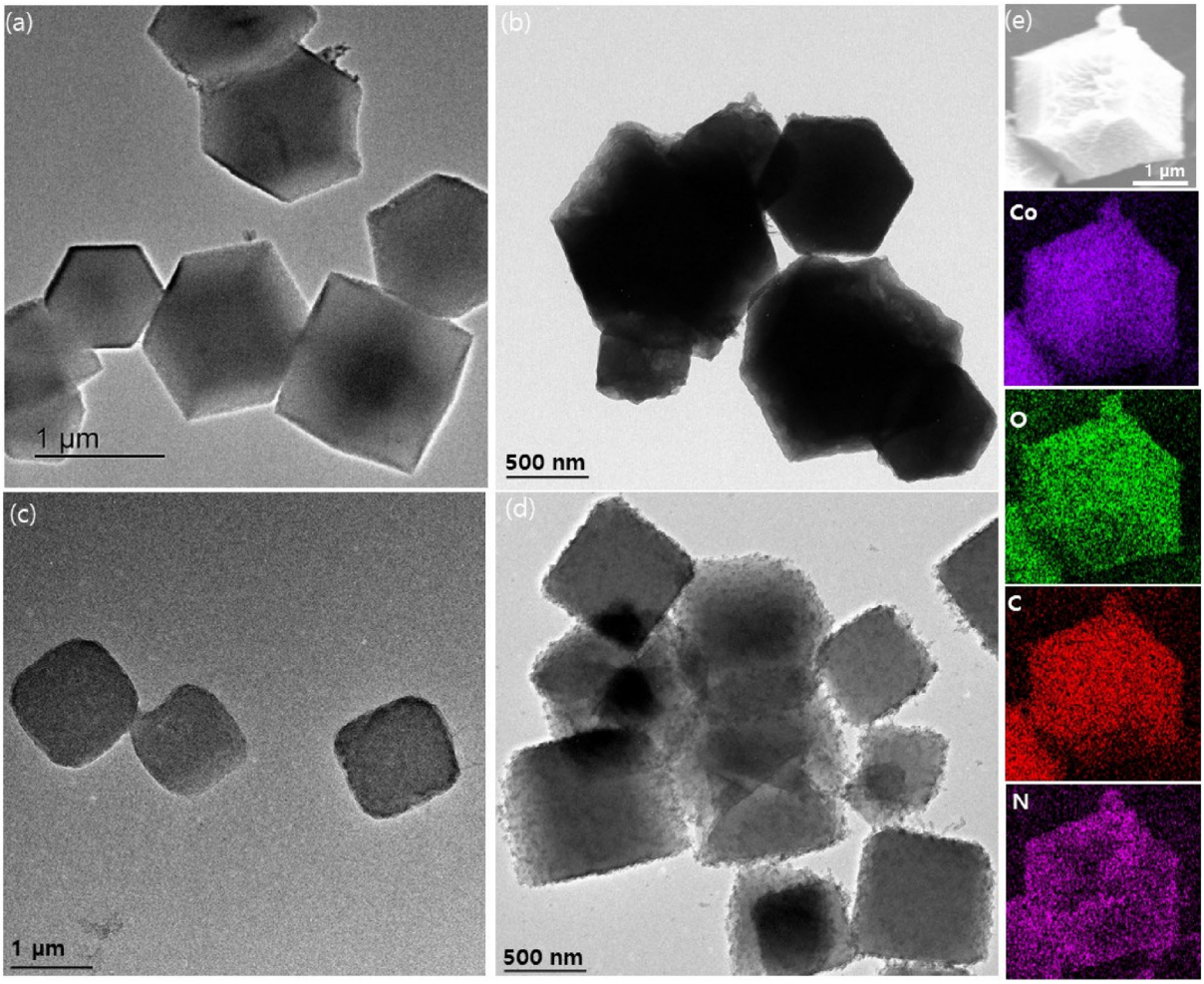

FIGURE 2 | **Electron microscopy investigation**. TEM image of undoped Co_3O_4-NC1 (a) and doped Co_3O_4-NC1 (b) and corresponding undoped Co_3O_4-NC2 (c) and doped Co_3O_4-NC2 (d), EDS elemental mapping of Co_3O_4-NC1 Pc (e).

(TEM) images of Co_3O_4-NC1 and corresponding Co_3O_4-NC1 Pc, while Figure 2c,d shows the TEM images of Co_3O_4-NC2 and the corresponding Co_3O_4-NC2 Pc.

The TEM analysis reveals no significant change in morphology following CoPc doping, but more aggregated structures are observed (Figure 2b,d), which could be attributed to π-π interaction of the CoPc with the N-doped carbon framework. The representative elemental mapping obtained with energy-dispersive X-ray spectroscopy of Co_3O_4-NC2 Pc shows uniform distribution of expected elements within the structure (Figure 2e). The representative high-resolution TEM (HRTEM) images of Co_3O_4-NC1 Pc and Co_3O_4-NC2 Pc are shown in Figure 3a,b. A fast Fourier transform (FFT) and its inverse (IFFT) were performed in the delineated regions of the HRTEM using the Gatan Digital Micrograph software to facilitate a detailed examination of the interplanar distances of the samples. The observed IFFT lattice fringes with interplanar distances of 0.240 nm and 0.237 nm in Co_3O_4-NC1 Pc and Co_3O_4-NC2 Pc, respectively, correspond to (311) plane of Co_3O_4 [27].

The crystal structure of the as-prepared samples was investigated using X-ray diffraction (XRD). The XRD patterns of the polyhedron- and cubic-shaped MOF samples matched well with the simulated patterns (Figure S2).

The XRD of the CoPc alone displayed a broad peak between $2\theta = 20°–25°$ (Figure S3), which is consistent with the amorphous structure of phthalocyanines [28]. The XRD pattern of the MOF completely changed after annealing (Figure 4a and Figure S3) due to the breakdown of the organic linkers to form a porous carbon network and the oxidation of Co(II) ion to Co_3O_4 [29]. The observed prominent XRD peaks at $2\theta = 14.76°$, 31.41°, 36.92°, 45.01°, and 65.29° (Figure 4a and Figure S3) correspond to crystal indices of Co_3O_4 (111), (200), (311), (400), and (440) (JCPDS No. 42–1467). Compared to the undoped Co_3O_4-NC1 and Co_3O_4-NC2, a strong enhancement around 20°–25° in the doped derivatives indicates the presence of Pc in the material after doping.

X-ray photoelectron spectroscopy (XPS) was employed to understand the surface chemical state and coordination environment

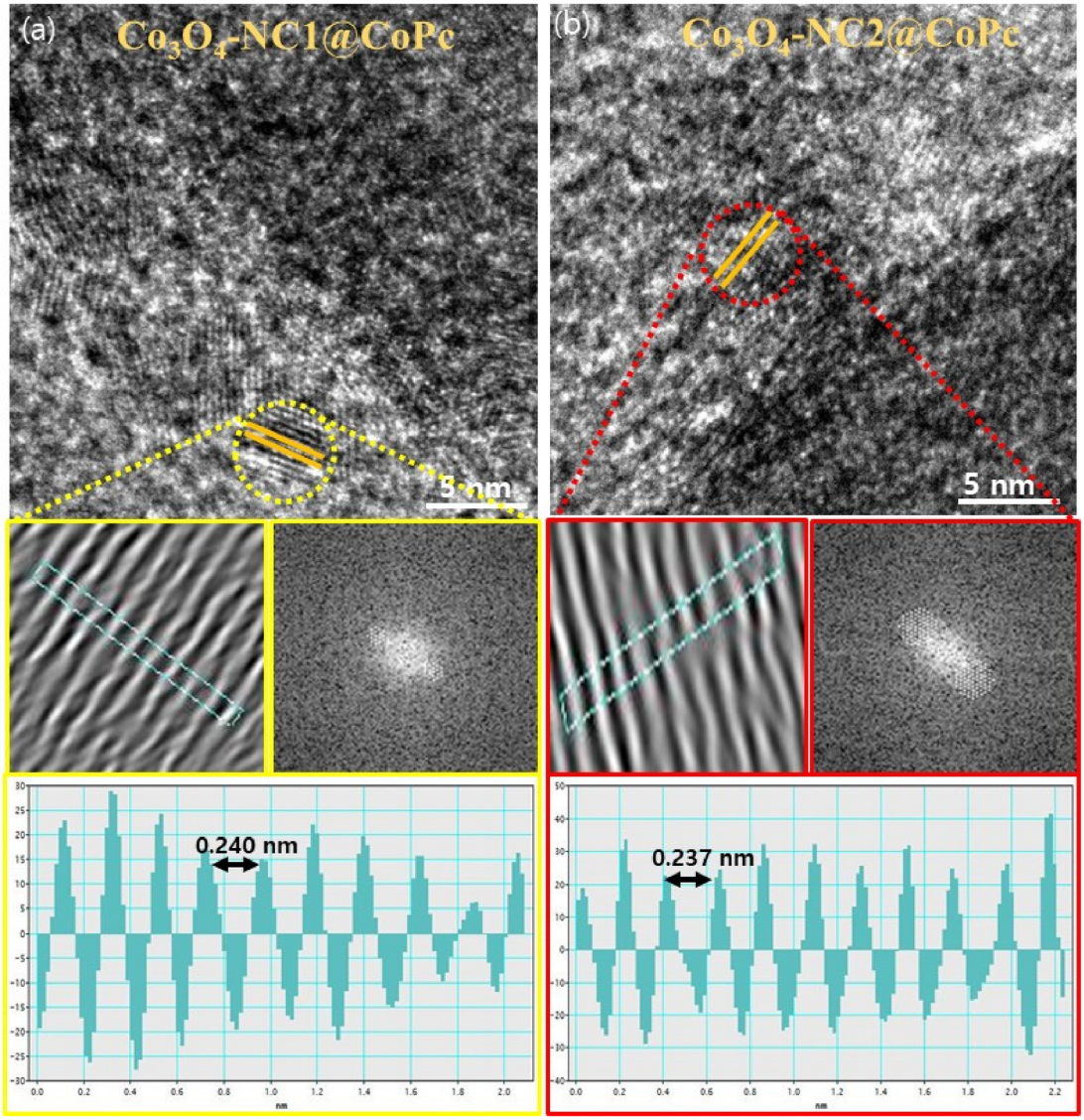

FIGURE 3 | HRTEM images of Co_3O_4-NC1 Pc (a) and Co_3O_4-NC2 Pc (b) with corresponding fast Fourier transform (FFT) and its inverse (IFFT) were performed in the delineated regions.

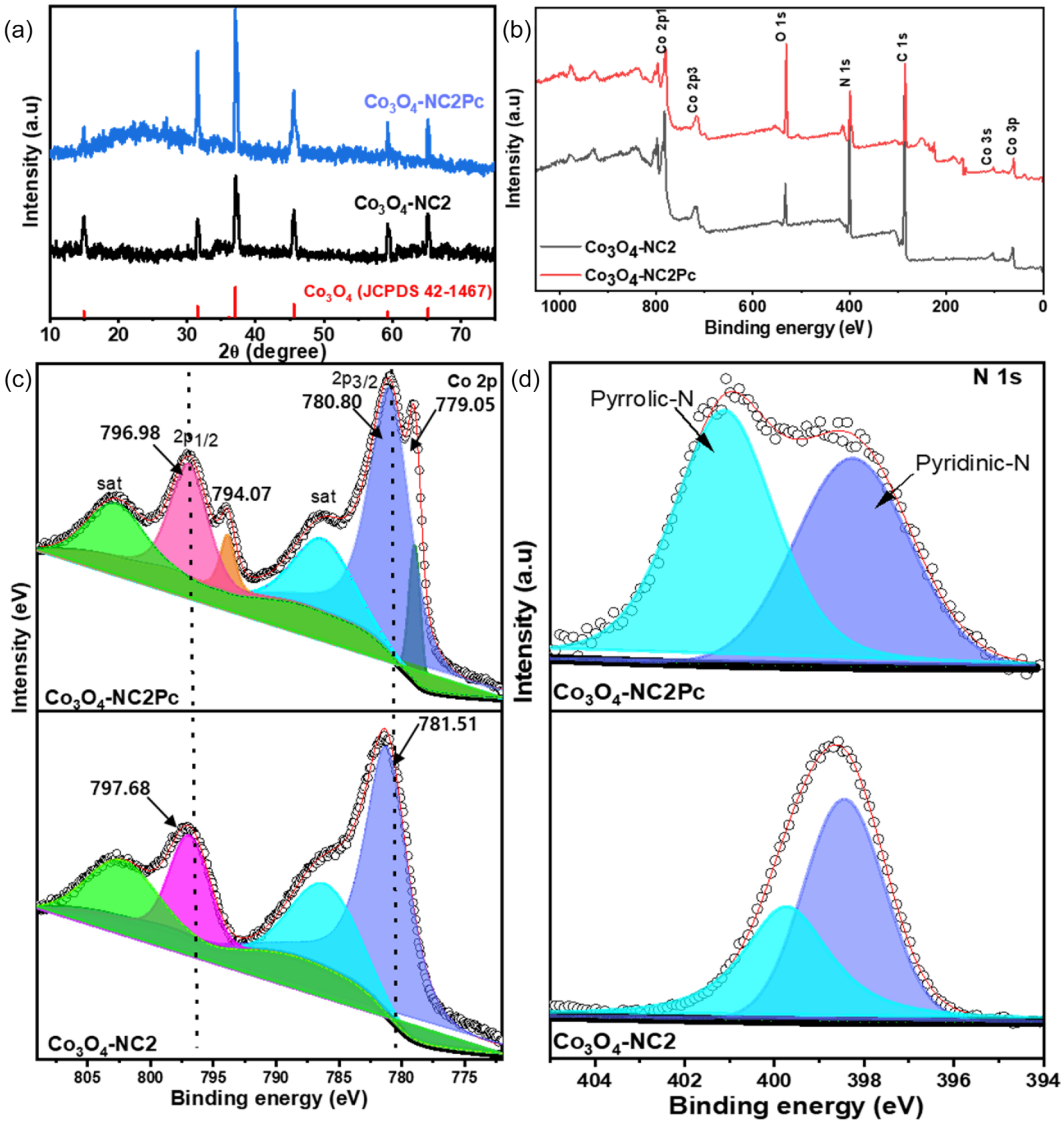

FIGURE 4 | **Structure and elemental state study**. (a) XRD pattern of undoped and doped Co_3O_4-NC2, (b) XPS survey spectra, and (c,d) high-resolution XPS spectra of the as-prepared samples.

of the elements. The XPS survey spectra (Figure 4b) reveal the presence of C, Co, O, and N in the samples as expected. The deconvoluted high-resolution XPS spectra are shown in Figure 4c,d and Figure S4. The deconvoluted Co 2p shows two spin–orbit doublet fitted to $2p_{3/2}$ and $2p_{1/2}$ orbitals, which correspond to + 2 and + 3 oxidation state of Co [30]. In addition to these doublet peaks, shake-up satellite peaks were also observed that can be associated with charge–transfer excitations from oxygen to the Co ion during the photoemission process [31].

Compared to the undoped Co_3O_4-NC2, the doped Co_3O_4-NC2 Pc shows two pairs of peaks in addition to the satellites (Figure 4c)

The first set of peaks occurs at binding 779.05 eV and 794.07 eV, while the second set of peaks is located at binding energies of 780.80 eV and 796.98 eV. This observation suggests the occurrence of a set of Co in different chemical environments and can be attributed to Co from the Co_3O_4 and Co coordinated to nitrogen of phthalocyanine. In addition, the Co 2p in Co_3O_4-NC2 shows a positive shift by ca. 0.7 eV compared to Co_3O_4-NC2 Pc, which could be attributed to inter-electron transfer between Co_3O_4-NC and CoPc [32]. The deconvolution of the N 1s spectra (Figure 4d) reveals the predominant presence of pyrrolic and pyridinic nitrogen species [33]. The deconvoluted O 1s spectra showed two subpeaks, which can be assigned to C-O and C═O in both doped and undoped materials (Figure S4), suggesting a similar oxygen coordination environment.

3.1 | Electrochemical Performance

To evaluate the electrocatalytic performance of the samples toward OER, we employed linear sweep voltammetry (LSV) using a typical three-electrode alkaline electrolyzer with Hg/HgO (1.0 M KOH) and graphite rods as a reference and counter electrode in 1.0 M KOH electrolyte.

The OER profile (Figure 5a, Figure S5a) shows a significant lowering in potential after doping with Pc. From the overpotential plot at 10, 100, and 1000 mA cm^{-2} (Figure 5b), the bare PC could not reach a current density of 1000 mA cm^{-2}. The Co_3O_4-NC2 Pc requires only 120, 210, and 435 mV to deliver a current density of

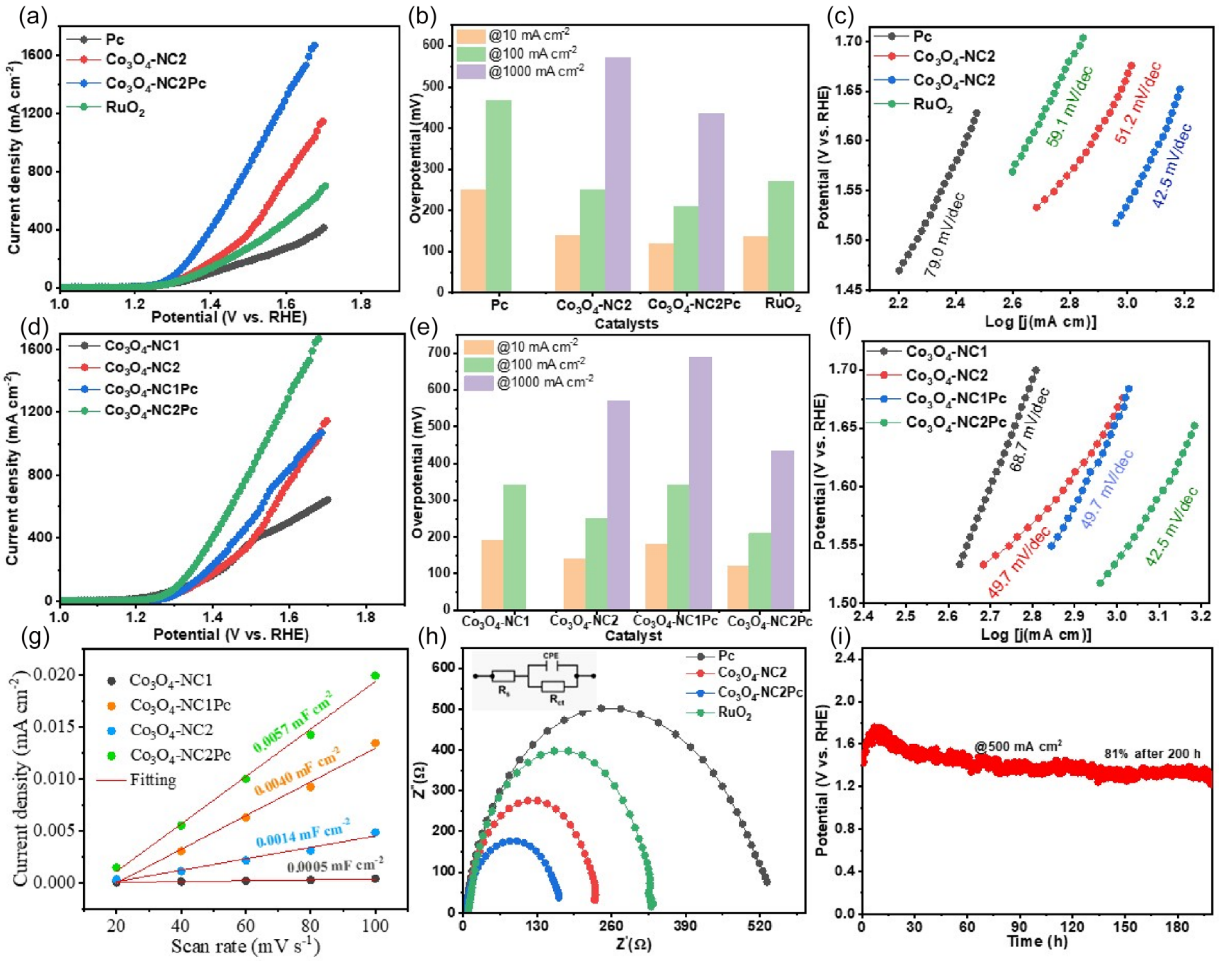

FIGURE 5 | Electrocatalytic performance. (a) LSV, (b) overpotential, (c) Tafel slope for CoPc, undoped Co_3O_4-NC_2, and corresponding doped derivatives relative to standard commercial RuO_2. (d) Comparative LSV, (e) overpotential, (f) Tafel slope for the polyhedron- and cubic-shaped based samples, (g) ECSA determination plots, (h) EIS Nyquist plots for the respective as-prepared samples, (i) chronopotentiometry stability profile of Co_3O_4-NC_2Pc over 200 h testing period at 500 mA cm^{-2}.

10, 100, and 1000 mA cm^{-2}, respectively, which is lower than 140, 250, and 540 mV required by Co_3O_4-NC2 to deliver the same current density. Compared to the state-of-the-art RuO_2, both Co_3O_4-NC2 Pc and Co_3O_4-NC2 required lower potential to deliver a current density of 100 and 1000 mA cm^{-2}, indicating superior catalytic performance. The Tafel plots (Figure 5c) of the electrode materials were used to obtain the kinetics of the OER. Analysis of the Tafel plot shows that the Co_3O_4-NC2 Pc possesses the lowest Tafel slope of 42.5 mV dec^{-1} compared to Co_3O_4-NC2 (49.7 mV dec^{-1}), RuO_2 (59.1 mV dec^{-1}), and Pc (79.0 mV dec^{-1}), suggesting its fast OER kinetics. Comparing the OER performance of samples derived from polyhedron- (i.e., Co_3O_4-NC1 and Co_3O_4-NC1 Pc) and cubic-shaped MOFs (Co_3O_4-NC2 and Co_3O_4-NC2 Pc), there is no significant variation in performance at current density of 10 and 100 mA cm^{-2} (Figure 5d). At an elevated current density of 1000 mA cm^{-2}, Co_3O_4-NC2 and Co_3O_4-NC2 Pc show a lowering of the potential. The overpotential at current density of 1000 mA cm^{-2} are in order of Co_3O_4-NC2 Pc (433 mV) < Co_3O_4-NC1 Pc (435 mV) < Co_3O_4-NC2 (570 mV), while Co_3O_4-NC1 could not reach the current density of 1000 mA cm^{-2}. The Co_3O_4-NC2 Pc shows superior or comparative performance compared to related materials previously reported (Table S1). The enhanced catalytic performance by Co_3O_4-NC2 derivatives could be attributed to either enhanced electrochemical surface area or the presence of more defects that facilitate reaction kinetics. To further probe this enhanced performance, we carry out further analysis using the catalyst's electrochemical surface area (ECSA), since the evaluation of catalytic performance using geometric current density consists of several parameters [34], as well as electron paramagnetic resonance measurement to have insight into the presence of vacancy, which increases defects. The CV profile of the samples at the non-Faradaic region is presented in Figure S6, and the double layer capacitance (C_{dl}) plots derived from the cyclic voltammetry (CV) as an excellent indicator of electrochemical surface area (ECSA) are shown in Figure 5g. Co_3O_4-NC2 Pc showed a C_{dl} value of 0.0057 mF cm^{-2}, which is more than 1.5-fold higher than that of Co_3O_4-NC1 Pc (0.004 mF cm^{-2}) and largely greater than the C_{dl} of 0.0014 and 0.005 mF cm^{-2} for Co_3O_4-NC2 and Co_3O_4-NC1, respectively, indicating significant enhancement in the active surface area. The increase in electrochemical surface area (ECSA) usually results in exposure of the more catalytically active sites and enhances the catalytic performance [35, 36]. Additionally, the EPR study revealed a greater than 1.5-fold improvement in the vacancy-related resonance signal for the Co_3O_4-NC2 Pc compared to Co_3O_4-NC1 Pc, with the Gauss factor

(g) detected between $g = 2.018$ and 2.022 (Figure S7). This indicates that Co_3O_4-NC2 Pc not only possesses an enhanced electrochemically active area but also possesses the presence of more vacant sites that facilitate electrochemical reaction kinetics. A CTAB and π-π stacking-induced vacancy has been previously reported [37, 38]. Thus, the enhanced vacancy following Pc incorporation could be attributed to the π-π stacking of the Pc onto Co_3O_4 surface. Given that CTAB was used to alter the morphology from polyhedron to cubic shape, the synergistic interaction of CTAB and π-π stacking could enhance the vacancy-related signal; hence, Co_3O_4-NC2 Pc exhibits enhanced vacancy signal compared to Co_3O_4-NC1 Pc.

The charge transfer mechanism of the electrode reactions was investigated using electrochemical impedance spectroscopy (EIS) (Figure 5h). An equivalent circuit for recreating the EIS data is shown as inserted in Figure 5h and was used for better understanding of the electrocatalytic mechanisms at play in catalysts. The charge transfer resistance (R_{ct}) for Co_3O_4-NC2 Pc, Co_3O_4-NC2, RuO_2, and Pc are 4.92 Ω, 6.8 Ω, 9.6 Ω, and 10.1 Ω, respectively, indicating a lower resistance for Co_3O_4-NC2 Pc that facilitates efficient catalytic performance. The chronopotentiometric measurements were used to study the stability of Co_3O_4-NC2 Pc at an applied current of 500 mA cm^{-2} (Figure 5i). The long-term stability test for 200 h shows a negligible change of current density with high current retention of 80%, which indicates efficient stability of the material. The post stability SEM and XRD of Co_3O_4-NC2 Pc are shown in Figure S8a–c. The SEM image after stability test (Figure S8b) shows no significant change in morphology, but the particles become aggregated, which can be attributed to electrolyte-induced aggregation. The XRD after analysis after stability test (Figure S8c) reveals that the structural integrity of the catalyst as the crystalline peak of Co_3O_4-NC and

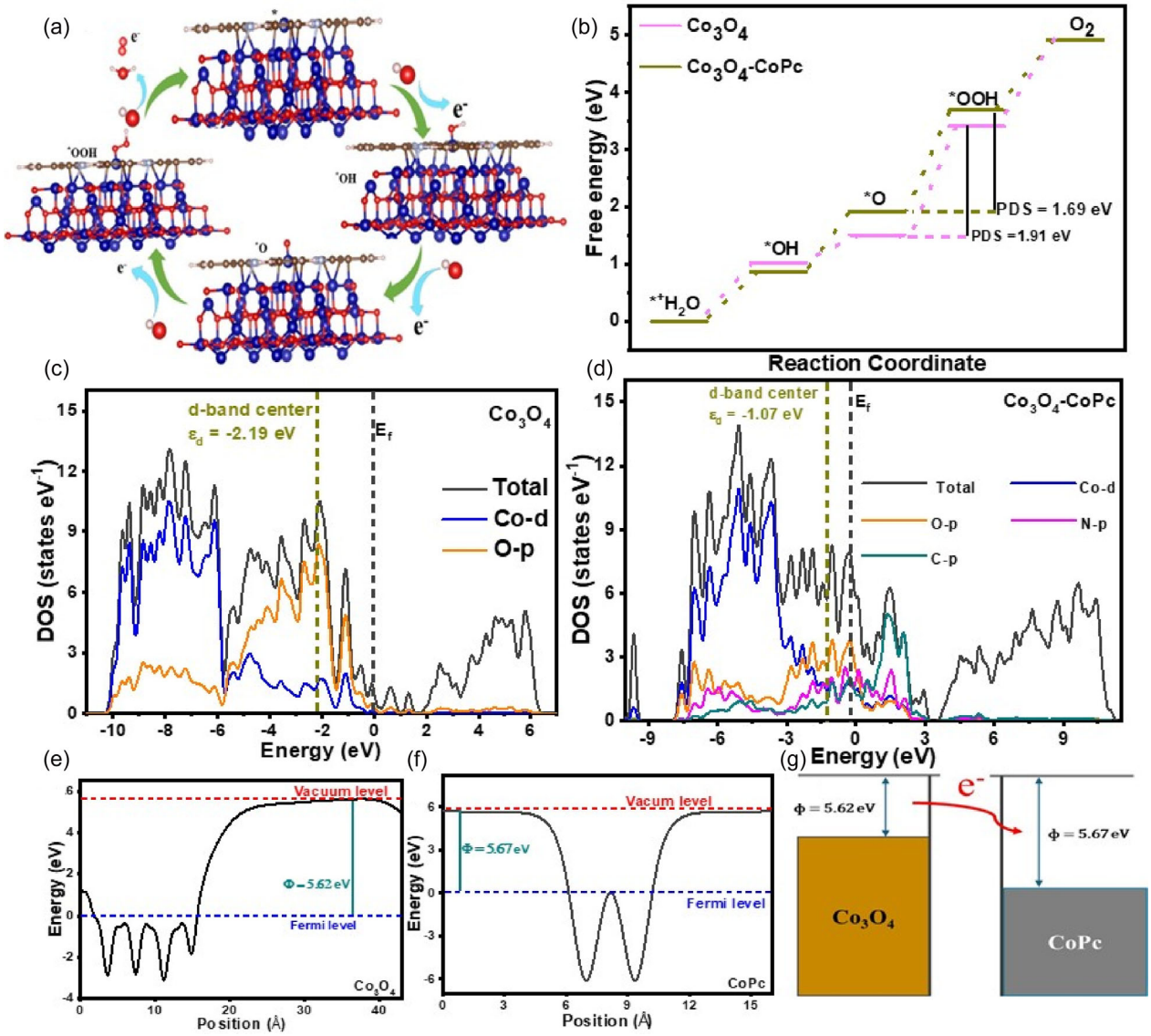

FIGURE 6 | Mechanistic investigation. (a) Optimized adsorption structures of reaction intermediates on Co active sites of Co_3O_4-CoPc, showing electron transfer processes during catalysis, (b) Free energy diagrams for the oxygen evolution reaction (OER) with potential-determining steps (PDS) for Co_3O_4 and Co_3O_4-CoPc, (c,d) The calculated projected density of states (PDOS) of Co_3O_4 and Co_3O_4-CoPc, (e,f) The calculated work function diagrams of Co_3O_4 and CoPc, and (g) the electron transfer diagram between Co_3O_4 and CoPc, respectively.

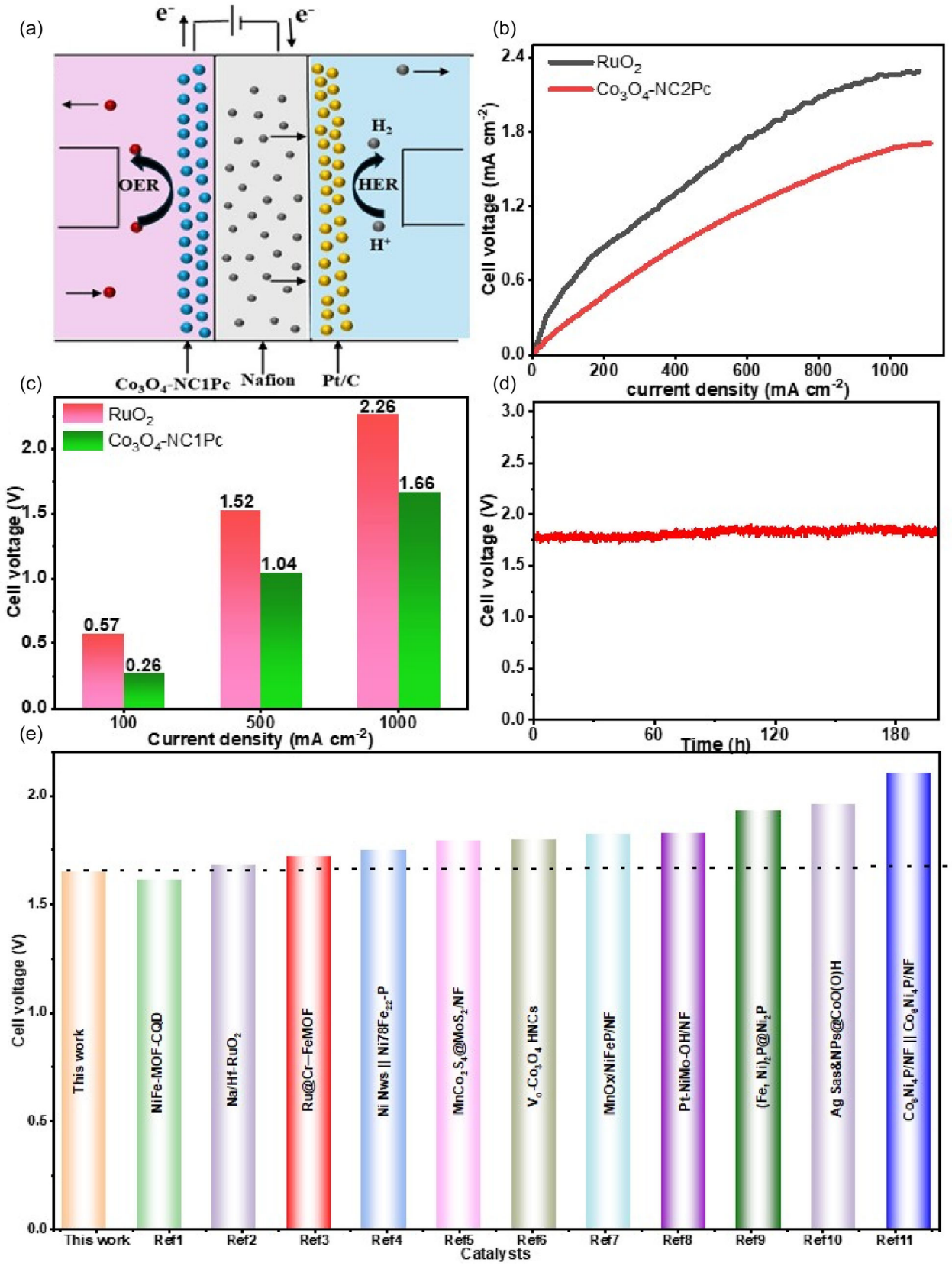

FIGURE 7 | **Electrochemical overall water splitting study**. (a) Schematic illustration of the proton exchange membrane electrode construction, (b) LSV curve of PEM water electrolyzer, (c) overpotential of the PEM device at different current densities, (d) the chronopotentiometry test of Co_3O_4-NC2 Pc electrolyzer at 1000 mA cm^{-2} for 200 h, (e) comparison of Co_3O_4-NC2 Pc performance at the current density of 1000 mA cm^{-2} with the literature data.

the amorphous peak of Pc were maintained at their respective positions, but with weakened intensity. The weakening of intensity suggests slight degradation of the material. Also, the OER conducted after the stability test does not show significant variation in performance (Figure S9).

3.2 | DFT Study

The electrocatalytic effect toward OER, arising from synergistic effects of interaction of CoPc with Co_3O_4, was investigated using DFT. The optimized computational models of the Co_3O_4 (311) and Co_3O_4-CoPc hetero-interface are shown in Figure S10. The dependence of catalytic performance of the proposed nanostructures and the Gibbs free energy difference (ΔG) of the active sites and intermediates (OH*, O*, and OOH* radicals) are well-known phenomena [39, 40]. The optimized structures for the adsorption of intermediate and mechanistic pathway during OER on Co_3O_4-CoPc and Co_3O_4 are shown in Figure 6a and Figure S11, respectively, while Figure 6b depicts the free energy diagrams arising from the OER on Co_3O_4 and Co_3O_4-CoPc catalysts. The free energy diagrams reveal that the formation of OOH* is the rate-determining step (RDS) in both cases. The Gibbs free energy difference (ΔG) of Co_3O_4 (1.91 eV) is higher than that of Co_3O_4-CoPc (1.69 eV), suggesting that Co_3O_4-CoPc requires a lower overpotential to drive water oxidation, hence possessing better catalytic performance. Additionally, we computed the electronic structures of Co_3O_4 and Co_3O_4-CoPc using the DFT + U method (Figure 6c,d) to gain a deeper insight into the effect of CoPc doping impact. The partial density of state (PDOS) analysis of the composite Co_3O_4-CoPc reveals additional contributions from N-p and C-p states, with significant enhancement in the PDOS at the Fermi energy (E_f) level, indicating that more charge carriers participate in the catalytic reaction, which could enhance catalytic performance, electrical conductivity, and charge transfer kinetics [41, 42]. Moreover, the work functions of Co_3O_4 and Co_3O_4-CoPc were calculated (Figure 6e,f) to gain a deeper insight into the electron transfer pathway and the underlying reasons for enhanced electrochemical performance in the Co_3O_4-CoPc. The result shows that the work functions of Co_3O_4 and CoPc were 5.62 eV and 5.67 eV, respectively, which suggests electron transfer from Co_3O_4 to CoPc as shown in Figure 6g, which results in an electron deficit near Co_3O_4 and a surplus near CoPc.

Under this condition, the electron-rich core of CoPc promotes the adsorption of oxygen-containing intermediate bonds, leading to improved electrochemical performance.

Water electrolysis via proton exchange membrane (PEM) is a promising hydrogen production technology approach [43, 44]. We assessed the potential for industrial application of Co_3O_4-NC2 Pc for water electrolysis by using it as an anode catalyst for OER with Nafion 115 as membrane separator and commercial Pt/C as a cathode for hydrogen evolution reaction (HER), as shown in Figure 7a, Figure S12. The catalyst loading in the anode and cathode is 3.0 mg cm^{-2} and 0.3 mg cm^{-2}, respectively, and the effective electrode area is 60 cm^2. Figure 7b shows the plot of current–voltage (I–V) profile of the electrolyzer using Co_3O_4-NC2Pc//Pt/C in comparison with commercial RuO_2//Pt/C. The polarization curve shows that Co_3O_4-NC2Pc//Pt/C pair requires a lower cell voltage of 1.66 V to achieve the industrial value of 1.0 A cm^{-2}, which is superior to RuO_2//Pt/C electrode pair that requires 2.26 V to deliver the same current density (Figure 7c), indicating the high catalytic potential of Co_3O_4-NC2 Pc for real-world application in water splitting [45].

In practical applications, stability is a critical factor—even more so than its catalytic activity. We put the Co_3O_4-NC2 Pc-based electrolyzer through its stability test by conducting a long-term electrolysis for 200 h under industrially relevant high-current conditions of 1.0 A cm^{-2}. Figure 7d shows that the electrolyzer can maintain a stable voltage of around 1.7 V for over 200 h at a constant current density of 1.0 A cm^{-2}, confirming the potential of the Co_3O_4-NC2 Pc catalyst as excellent OER stability under real-operating conditions. The comparative performance of our catalysts with other reported catalysts recorded at 1 A cm^{-2} showed superior or comparable catalytic performance by our catalysts (Figure 7e).

4 | Conclusion

In conclusion, we employed a facile, template-assisted synthetic approach to preparing CoPc-doped Co_3O_4-NC exhibiting high electrooxidation activity toward OER. The innovative catalyst was further applied in industrial PEM water electrolysis, showcasing outstanding performance. DFT calculations revealed that the synergistic interaction of Co_3O_4-NC and CoPc enhances fast electron transfer and optimizes the electronic structure, which improved electron transport significantly and boosted the OER performance. The Co_3O_4-NC2 Pc composite demonstrated exceptional performance, achieving a current density of 1000 mA cm^{-2} with a significantly reduced overpotential of just 1.53 V, which is notably lower than the 1.67 V required by Co_3O_4-NC2 alone, indicating the importance of doping with CoPc for enhancing catalytic performance. Additionally, Co_3O_4-NC2 Pc showed a larger C_{dl} value, indicating a larger ECSA and more active catalytic sites, which are favorable for the OER process. When applying as anode catalyst in the PEM electrolyzer, Co_3O_4-NC2 Pc demonstrated remarkable performance, requiring only 1.66 V to reach industrial-level current densities of 1.0 A cm^{-2}. Moreover, under an applied current of 1 A cm^{-2}, the cell voltage was maintained around 1.7 V for over 200 h, demonstrating the excellent electrochemical activity and long-term stability of the electrode device. This research accomplishment not only propels the facile synthetic approach but also establishes a robust foundation for the advancement of hydrogen energy production and chemical industries, thereby establishing a landmark for the implementation of the material catalyst in industrial-scale PEM water electrolysis.

Acknowledgments

This work was supported by the National Science Foundation under grant program International Research Experience for Students (NSF IRES 21072201 SOLARIS), the National Research Foundation of Korea (NRF) 2021K1A3A1A16096990 and 2019K1A3A1A18116066, grant funded by the Korea government (MSIT) number RS-2023–00219710 and RS-2024–00333541; Industrial Strategic Technology Development Program, grant number 20025720, funded by the Ministry of Trade, Industry & Energy (MOTIE, Korea). 00219710) and Ministry of Trade, Industry and Energy of Korea (no. 20025720). A.R. would like to thank

the National Science Centre of Poland (NCN) through Miniatura grant number 2024/08/X/ST11/00346. C.G. and J.T. thank the 2024 Summer School on nanomaterials at IPPT, PAN, Poland.

Funding

National Science Foundation under grant program International Research Experience for Students (NSF IRES 21072201 SOLARIS).

Conflicts of Interest

The authors declare no conflicts of interest.

Data Availability Statement

The data that support the findings of this study are available from the corresponding author upon reasonable request.

References

1. J. Xie, S. Wang, H. Luo, et al., "Reconstruction of CoNx/NC Catalyst during Oxygen Evolution Reaction by Fe3+ Modulation for Enhanced Activity and Stability," *ChemSusChen* 10 (2017): 3268–3275.

2. H. Tong, Y. Jiang, Q. Zhang, et al., "Enhanced Interfacial Charge Transfer on a Tungsten Trioxide Photoanode with Immobilized Molecular Iridium Catalyst," *ChemSusChem* 10 (2017): 3268–3275.

3. S. Cui, M. Qian, X. Liu, Z. Sun, and P. Du, "A Copper Porphyrin-Based Conjugated Mesoporous Polymer-Derived Bifunctional Electrocatalyst for Hydrogen and Oxygen Evolution," *ChemSusChem* 9 (2016): 2365–2373.

4. J. Qi, N. Benipal, H. Wang, et al., "Metal-Catalyst-Free Carbohydrazide Fuel Cells with Three-Dimensional Graphene Anodes," *ChemSusChem* 8 (2015): 1147–1150.

5. B. Qiu, A. Han, D. Jiang, T. Wang, and P. Du, "Cobalt Phosphide Nanowire Arrays on Conductive Substrate as an Efficient Bifunctional Catalyst for Overall Water Splitting," *ACS Sustainable Chemistry & Engineering* 7, no. 2 (2018): 2360–2369, https://doi.org/10.1021/acssuschemeng.8b05137.

6. S. Chakrabarty, A. Mukherjee, and S. Basu, "RGO-MoS_2 Supported $NiCo_2O_4$ Catalyst toward Solar Water Splitting and Dye Degradation," *ACS Sustainable Chemistry & Engineering* 6, no. 4 (2018): 5238–5247, https://doi.org/10.1021/acssuschemeng.7b04757.

7. S. Cherevko, S. Geiger, O. Kasian, et al., "Oxygen and Hydrogen Evolution Reactions on Ru, RuO2, Ir, and IrO2 Thin Film Electrodes in Acidic and Alkaline Electrolytes: A Comparative Study on Activity and Stability," *Catalysis Today* 262 (2016): 170–180, https://doi.org/10.1016/j.cattod.2015.08.014.

8. S. Trasatti, "Electrocatalysis by Oxides—Attempt at a Unifying Approach," *Journal of Electroanalytical Chemistry and Interfacial Electrochemistry* 111, no. 1 (1980): 125–131, https://doi.org/10.1016/S0022-0728(80)80084-2.

9. X. Zou and Y. Zhang, "Noble Metal-Free Hydrogen Evolution Catalysts for Water Splitting," *Chemical Society Reviews* 44, no. 15 (2015): 5148–5180, https://doi.org/10.1039/C4CS00448E.

10. D. Strmcnik, M. Uchimura, C. Wang, et al., "Improving the Hydrogen Oxidation Reaction Rate by Promotion of Hydroxyl Adsorption," *Nature Chemistry* 5, no. 4 (2013): 300–306, https://doi.org/10.1038/nchem.1574.

11. G. Chen, H. Li, Y. Zhou, et al., "CoS2 Needle Arrays Induced a Local Pseudo-Acidic Environment for Alkaline Hydrogen Evolution," *Nanoscale* 13, no. 32 (2021): 13604–13609, https://doi.org/10.1039/D1NR03221F.

12. Q. Zhou, Y. Chen, G. Zhao, et al., "Active-Site-Enriched Iron-Doped Nickel/Cobalt Hydroxide Nanosheets for Enhanced Oxygen Evolution Reaction," *ACS Catalysis* 8, no. 6 (2018): 5382–5390, https://doi.org/10.1021/acscatal.8b01332.

13. X. Yuan, T. Yan, Z. Liu, and P. Kang, "Highly Efficient Alkaline Water Electrolysis Using Alkanolamine-Functionalized Zirconia-Blended Separators," *ACS Sustainable Chemistry & Engineering* 11, no. 10 (2023): 4269–4278, https://doi.org/10.1021/acssuschemeng.2c07618.

14. X. Zhang, M. Jin, F. Jia, et al., "Noble-Metal-Free Oxygen Evolution Reaction Electrocatalysts Working at High Current Densities over 1000 mA cm^{-2} : From Fundamental Understanding to Design Principles," *Energy and Environmental Materials* 6, no. 5 (2023): e12457, https://doi.org/10.1002/eem2.12457.

15. J. Ding, Y. Tang, S. Zheng, et al., "The Synthesis of MOF Derived Carbon and Its Application in Water Treatment," *Nano Research* 15, no. 8 (2022): 6793–6818, https://doi.org/10.1007/s12274-022-4327-1.

16. Q. Li, Z. Dai, J. Wu, et al., "Fabrication of Ordered Macro-Microporous Single-Crystalline MOF and Its Derivative Carbon Material for Supercapacitor," *Advanced Energy Materials* 10 (2020): 33, https://doi.org/10.1002/aenm.201903750.

17. X. Lin, J. Xu, and Z. Peng, "Atomically Dispersed Catalysts toward the Oxygen Evolution Reaction in Electrochemical Water Splitting: From Catalyst Design, Performance to Catalytic Mechanism," *Next Sustainability* 3 (2024): 100023, https://doi.org/10.1016/j.nxsust.2023.100023.

18. N. Nwaji, J. Mack, and T. Nyokong, "Photophysical and Strong Optical Limiting Properties of Ball-Type Phthalocyanines Dimers and Their Monomeric Analogues," *Journal of Photochemistry and Photobiology A: Chemistry* 352 (2018): 73–85, https://doi.org/10.1016/j.jphotochem.2017.10.045.

19. Z.-y. Mei, S. Cai, G. Zhao, et al., "Boosting the ORR Active and Zn-Air Battery Performance through Ameliorating the Coordination Environment of Iron Phthalocyanine," *Chemical Engineering Journal* 430 (2022): 132691, https://doi.org/10.1016/j.cej.2021.132691.

20. W. Xia, Z. Hou, J. Tang, et al., "Materials Informatics-Guided Superior Electrocatalyst: A Case of Pyrolysis-Free Single-Atom Coordinated with N-Graphene Nanomesh," *Nano Energy* 94 (2022): 106868, https://doi.org/10.1016/j.nanoen.2021.106868.

21. X. Yu, S. Lai, S. Xin, et al., "Coupling of Iron Phthalocyanine at Carbon Defect Site via π-π Stacking for Enhanced Oxygen Reduction Reaction," *Applied Catalysis B: Environmental* 280 (2021): 119437, https://doi.org/10.1016/j.apcatb.2020.119437.

22. X. Wang, A. Dong, Y. Hu, J. Qian, and S. Huang, "A Review of Recent Work on Using Metal–organic Frameworks to Grow Carbon Nanotubes," *Chemical Communications* 56, no. 74 (2020): 10809–10823, https://doi.org/10.1039/D0CC04015K.

23. J. Yao, M. He, and H. Wang, "Strategies for Controlling Crystal Structure and Reducing usage of Organic Ligand and Solvents in the Synthesis of Zeolitic Imidazolate Frameworks," *CrystEngComm* 17, no. 27 (2015): 4970–4976, https://doi.org/10.1039/C5CE00663E.

24. R. Matshitse, N. Nwaji, M. Mananga, E. Prinsloo, and T. Nyokong, "Effect of Number of Positive Charges on the Photophysical and Photodynamic Therapy Activities of Quarternary Benzothiazole Substituted Zinc Phthalocyanine," *Journal of Photochemistry and Photobiology A: Chemistry* 367 (2018): 253–260, https://doi.org/10.1016/j.jphotochem.2018.08.033.

25. Y.-Q. Zhang, M. Liu, L.-T. Zhang, et al., "Strategic Defect Engineering Enabled Efficient Oxygen Evolution Reaction in Reconstructed Metal-Organic Frameworks," *Advanced Functional Materials* 35, no. 4 (2025): 2412406, https://doi.org/10.1002/adfm.202412406.

26. S. Daliran, A. R. Oveisi, C. W. Kung, et al., "Defect-Enabling Zirconium-Based Metal–organic Frameworks for Energy and Environmental Remediation Applications," *Chemical Society Reviews* 53, no. 12 (2024): 6244–6294, https://doi.org/10.1039/D3CS01057K.

27. X. Yang, Y. Wang, Y. Hu, et al., "Interior Supported Hierarchical TiO_2@Co_3O_4 Derived From MOF-on-MOF Architecture with Enhanced Electrochemical Properties for Lithium Storage," *ChemElectroChem* 6, no. 14 (2019): 3657–3666, https://doi.org/10.1002/celc.201900915.

28. N. Nwaji, J. Mack, and T. Nyokong, "An Optical Limiting Study in Aminophenoxy Substituted Phthalocyanine in the Presence of Semiconductor Quantum Dots," *Journal of Luminescence* 203 (2018): 247–256, https://doi.org/10.1016/j.jlumin.2018.06.044.

29. T. R. Kuo, H. T. Draviana, C. S. Hsu, et al., "Novel Synthesis of ZIF67 Derived Cobalt and Nickel Oxides Induced by Ammonium Tetrafluoroborate as Electroactive Material of Battery Supercapacitor Hybrids," *Journal of Energy Storage* 68 (2023): 107831, https://doi.org/10.1016/j.est.2023.107831.

30. N. Nwaji, J. Gwak, M. Goddati, et al., "Defect-Engineered $Fe_3C@NiCo_2S_4$ Nanospike Derived From Metal-Organic Frameworks as an Advanced Electrode Material for Hybrid Supercapacitors," *ACS Applied Materials & Interfaces* 15 (2023): 34779, https://doi.org/10.1021/acsami.3c04635.

31. J. G. Dillard and M. H. Koppelman, "X-Ray Photoelectron Spectroscopic (xps) Surface Characterization of Cobalt on the Surface of Kaolinite," *Journal of Colloid and Interface Science* 87, no. 1 (1982): 46–55, https://doi.org/10.1016/0021-9797(82)90370-8.

32. Y. Sivalingam, G. Magna, R. Kalidoss, et al., "Combinatorial Selectivity with an Array of Phthalocyanines Functionalized TiO_2/ZnO Heterojunction Thin Film Sensors," *Nanotechnology* 33 (2021): 075503.

33. D. Chen, Q. Huang, J. Ding, et al., "Heteroepitaxial Metal-Organic Frameworks Derived Cobalt and Nitrogen Codoped Carbon Nanosheets to Boost Oxygen Reduction," *Journal of Colloid and Interface Science* 623 (2022): 1210–1219, https://doi.org/10.1016/j.jcis.2022.05.076.

34. N. K. Shrestha, S. A. Patil, J. Han, et al., "Chemical Etching Induced Microporous Nickel Backbones Decorated with Metallic Fe@hydroxide Nanocatalysts: An Efficient and Sustainable OER Anode toward Industrial Alkaline Water-Splitting," *Journal of Materials Chemistry A* 10, no. 16 (2022): 8989–9000, https://doi.org/10.1039/D1TA10103J.

35. N. Nwaji, B. Fikadu, M. Osial, et al., "Atomically Dispersed Ruthenium in Transition Metal Double Layered Hydroxide as a Bifunctional Catalyst for Overall Water Splitting," *Renewable Energy* 235 (2024): 121307, https://doi.org/10.1016/j.renene.2024.121307.

36. N. Nwaji, B. Fikadu, M. Osial, et al., "Disentangling the Catalytic Origin in Defect Engineered 2D $NiCoMoS@Ni(CN)_2$ Core-Shell Heterostructure for Energy-Saving Hydrazine-Assisted Water Oxidation," *International Journal of Hydrogen Energy* 86 (2024): 554–563, https://doi.org/10.1016/j.ijhydene.2024.08.432.

37. Y. Zou, Y. Ma, Y. Shi, et al., "Frozen" π-π Stacking on Perylene Diimide Molecules Induces Oxygen Vacancies Synergistic Activation of Persulfate towards Degradation of Tetracycline," *Chemical Engineering Journal* 496 (2024): 153852.

38. X. Han, J. Chen, L. Bao, H. Zhang, and Y.-J. Yuan, "CTAB-Induced Oxygen Vacancies and Z-Scheme Heterojunctions in $Bi_4O_5Br_2$ /BiOBr Ultrathin Nanosheets for Enhanced Photocatalytic Nitrogen Fixation," *ACS Applied Nano Materials* 8, no. 28 (2025): 14320–14327.

39. C. Ni, H. Zheng, W. Liu, et al., "Linker Defects in Metal–Organic Frameworks for the Construction of Interfacial Dual Metal Sites with High Oxygen Evolution Activity," *Advanced Functional Materials* 33, no. 25 (2023): 2301075, https://doi.org/10.1002/adfm.202301075.

40. X. Wang, W. Zhou, S. Zhai, et al., "Metal-Organic Frameworks: Direct Synthesis by Organic Acid-Etching and Reconstruction Disclosure as Oxygen Evolution Electrocatalysts," *Angewandte Chemie International Edition* 63, no. 11 (2024): e202400323, https://doi.org/10.1002/anie.202400323.

41. L. Zhang, Y. Jia, G. Gao, et al., "Graphene Defects Trap Atomic Ni Species for Hydrogen and Oxygen Evolution Reactions," *Chem* 4, no. 2 (2018): 285–297, https://doi.org/10.1016/j.chempr.2017.12.005.

42. S. Ye, F. Luo, Q. Zhang, et al., "Highly Stable Single Pt Atomic Sites Anchored on Aniline-Stacked Graphene for Hydrogen Evolution Reaction," *Energy & Environmental Science* 12, no. 3 (2019): 1000–1007, https://doi.org/10.1039/C8EE02888E.

43. Q. Ni, S. Zhang, K. Wang, et al., "Carbon Quantum Dot-Mediated Binary Metal Organic Framework Nanosheets for Efficient Oxygen Evolution at Ampere-Level Current Densities in Proton Exchange Membrane Electrolyzers," *Journal of Materials Chemistry A*. (2024): 31253–31261.

44. C. Liu, X. Cao, L. Chen, et al., "Synergistic Urea Oxidation and Hydrogen Evolution over MoC/Co/NCNT-Based Electrocatalysts for Cost-Effective Alkaline Electrolysis," *ACS Catalysis* 15, no. 17 (2025): 14983–14995.

45. X. Guo, H. Zhang, W. Xia, M. Ma, D. Cao, and D. Cheng, "Constructing Ag Single Atoms and Nanoparticles Co-Decorated CoO(O)H as Highly Active Electrocatalyst for Oxygen Evolution Reaction under Large Current Density," *Advanced Functional Materials* 34, no. 32 (2024): 2316539, https://doi.org/10.1002/adfm.202316539.

Supporting Information

Additional supporting information can be found online in the Supporting Information section.